ARMA 18–881

A method to assess potential induced seismicity hazard with application to the Duvernay

Lavoie, V.
Paramount Resources, Calgary, AB, Canada
Willson, S.M. & Sturm, C.
Apache Corporation, Houston, TX, USA
Lee, J. & Purdue, G.
Paramount Resources, Calgary, AB, Canada
Dempsey, D.
University of Auckland, Auckland, New Zealand

ABSTRACT: A workflow is presented to assess potential induced seismicity (IS) hazard associated with multi-well pad hydraulic fracturing stimulation, comprising steps of increasing sophistication which span easy-to-implement simple analytical screening tools to the application of a newly-developed model capable of calibrated forecasts of IS occurrence. The first level of hazard assessment takes a simplified fault description to determine stress changes required for the fault to become critically stressed. This permits a 'traffic light' screening of faults depending upon their slip potential. Extended analyses then incorporate fault surface topography and perturbations in stress and pressure caused by hydraulic fracturing operations. Potential IS event size is estimated using a fault size-magnitude relationship. These simplified assessments of fault slip potential are complemented by a more advanced consideration of fault rupture, fractal stress heterogeneity and evolving stress and pore pressure distributions. The advanced model provides a good qualitative match between the simulated and observed microseismic events occurring during well stimulation. Using the existing pad as a calibration point, 'what-if' scenarios are presented to assess operational procedures to minimize IS hazard and to assess IS potential in new areas ahead of well pad drilling and completion.

1. INTRODUCTION

It is now well-established that under certain geologic conditions the deep disposal of large volumes of water produced as part of oil and gas operations can trigger induced seismicity, IS (Ellsworth, 2013; Frohlich et al., 2014; Rubinstein and Babaie Mahani, 2015; Weingarten et al., 2015). More recently, there is also a growing awareness that hydraulic fracturing operations, too, can sometimes induce seismicity (Holland, 2011, 2013; B.C. Oil and Gas Commission, 2012, 2014; Davies et al., 2013; Friberg et al., 2013; Clarke et al., 2014; Skoumal et al., 2015; Atkinson, et al., 2016; Bao and Eaton, 2016; Schultz et al., 2017, 2018), even though the number of wells potentially associated with IS is exceptionally small – Table 1. However, within the Western Canada Sedimentary Basin, hydraulic fracturing has caused some of the largest IS events (Atkinson et al, 2016), and this has led the Alberta Energy Regulator (AER) to impose operational 'traffic light' protocols aimed at minimizing the risk of induced seismicity (AER, 2015, Figure 1).

Table 1. Comparison of occurrence rates for IS from disposal and HF – Ohio vs. Western Canada (Eaton et al., 2017).

Area	Wells	# Cases IS $M_L \geq 3$	%	Reference
Ohio	1400 HF	6	0.4	Skoumal et al., 2015
	200 Disposal	3	1.5	
Western Canada	12,300 HF	39	0.3	Atkinson et al., 2016
	1240 Disposal	17	1.4	

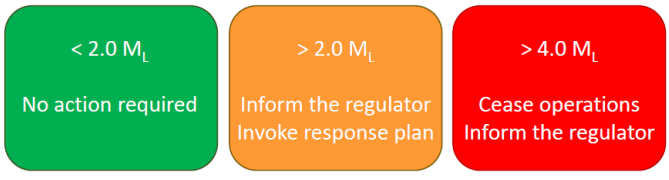

Fig. 1. IS traffic light system for the Fox Creek Duvernay Zone

Actions in response to events of magnitude 2.0M_L or greater typically include the reduction of injection rate and/or a reduction of injected volume. If a seismic event of 4.0 M_L or greater is detected in the vicinity of fracturing operations, the Operator must cease injection and consult with AER. In these circumstances, operations cannot

resume without AER consent. This can result in an entire well pad fracturing operation being shut-down for a considerable period of time, so leading to significant cost to the Operator.

In light of this, Operators are developing workflows to assess the potential hazard from IS. Current examples of these focus on the response to the significant hazard associated with waste water disposal – especially in Oklahoma, Kansas and Texas (Walters et al, 2015; Walsh and Zoback, 2016). Workflows for IS from hydraulic fracturing have, to date, been fairly high-level and focused on prudent monitoring practices (e.g. Green at al., 2012).

This paper seeks to redress the lack of specific guidelines for IS hazard assessment associated with hydraulic fracturing. A workflow is presented to assess potential hazard associated with multi-well pad stimulation. This comprises steps of increasing sophistication that span easy-to-implement simple analytical screening tools to the application of a newly-developed model capable of calibrated forecasts of IS occurrence.

It is recognized that the methodology for assessing IS caused by hydraulic fracturing is still a developing technology. It is anticipated that future developments will extend or supersede workflow tools described here. However, it is the Authors' hope that in publishing this paper added impetus will be given to the development of more robust screening and prediction tools.

2. DUVERNAY SECTION 26 WELL PAD

2.1. General Description

The Section 26 pad was drilled in 2015 in the Kaybob area targeting the Duvernay formation. The pad includes a vertical pilot well in the center and seven laterals of approximately 1200 m length which were drilled in a North-to-South direction (see Figure 2). Fracture stages were typically 75 m apart. The company successfully acquired data necessary to build a robust geomechanical model. The data set includes: core, full set of logs, Oil-Based Micro-Imager (OBMI), Diagnostic Formation Injection Tests (DFITs), downhole microseismic and moment tensor inversion on larger events.

2.2. Geomechanical Model

Determining the stress state in the Duvernay at the Section 26 location was aided by the availability of dipole sonic and density logging data; OBMI and several DFITs – from both the vertical data collection well and the toe stages of the Section 26 laterals. Rock mechanics test data were also available to calibrate rock strength, Young's Modulus and Poisson's Ratio. Pore pressure and minimum horizontal stress (Shmin) were therefore defined by the DFIT pressure-stress correlation applicable for this area.

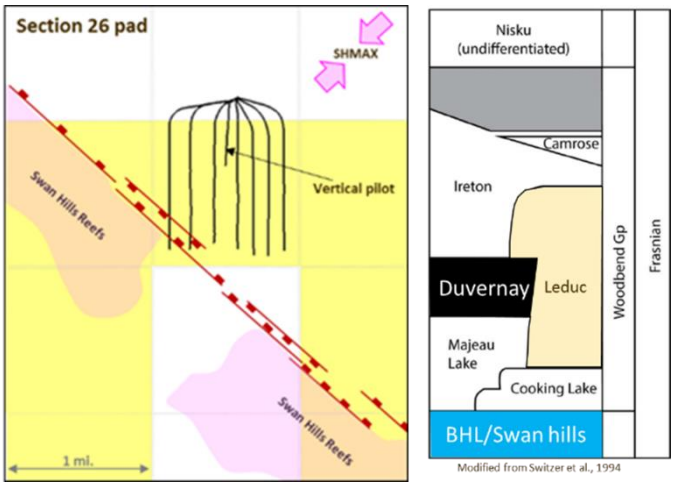

Fig. 2. Section 26 Pad layout schematic

Within the Duvernay interval the image log showed no breakouts or drilling-induced tensile fractures (DITFs). Using standard geomechanical analysis techniques (e.g. Zoback, 2010), estimates for maximum horizontal stress (SHmax) were made based on: (1) the magnitude of SHmax creating breakouts, and (2) the magnitude of SHMax resulting in DITFs. The final SHmax profile selected at any depth provides the maximum value that is consistent with both no breakouts and no DITFs.

For the appropriate landing zone depth (3100m TVD.RT) the following in-situ stress and pressure values were used in the analyses:

- Overburden = 76.29 MPa (24.61 kPa/m);
- Pore pressure = 53.84 MPa (17.37 kPa/m);
- Shmin = 57.65 MPa (18.60 kPa/m); and
- SHmax = 69.65 MPa (22.47 kPa/m)

These stress gradients, together with a N50°E maximum horizontal stress direction, are consistent with those reported by Bell and Grasby (2012). Focal mechanism inversions for larger microseismic events coinciding with stiffer limestone intervals are consistent with an oblique normal mechanism with a significant strike-slip component, consistent with the findings of Eaton and Babaie Mahani (2015).

3. STRESS & PORE PRESSURE CHANGES ARISING FROM HYDRAULIC FRACTURING

3.1. Stress Changes

Key to the assessment of IS hazard from hydraulic fracturing is the quantification of stress and pore pressure changes arising from these operations. As noted previously, these effects have not hitherto been explicitly included in IS assessments. They have, however, been used to quantify stage-to-stage interaction effects during hydraulic fracturing operations (Soliman and Adams, 2004; Roussel and Sharma, 2011; Roussel, 2017).

In total, excluding toe DFITs, a total of 112 frac stages were successfully placed in the seven Section 26 laterals. For each well the average build-up in instantaneous shut-in pressure (ISIP) was 8 MPa (Figure 3).

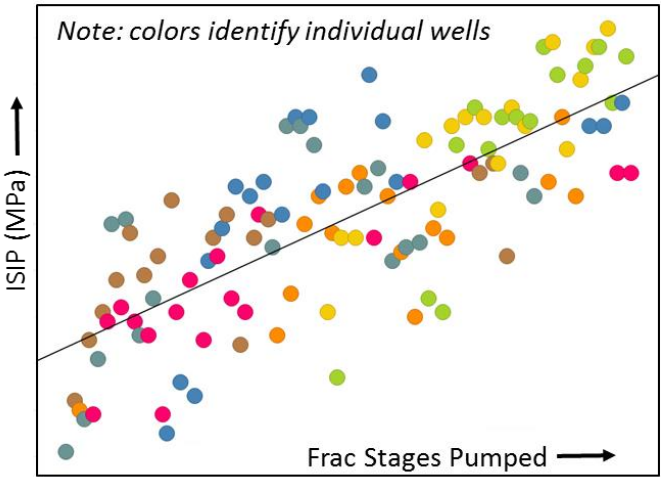

Fig. 3. ISIP build-up during zipper fracturing operations

The impact that this observed stress build-up has over the general pad area can be assessed using the well-established 'stress shadow' equations (Sneddon and Elliott, 1946; Sneddon, 1946; Yew and Weng, 2014), see Figure 4.

Two departures from the standard implementation of the stress shadow equations were implemented. First, angles were defined using the Cosine Rule, rather than as arctan expressions common in standard texts (e.g. Yew and Wang, 2014). This overcomes the 'division by zero' problem in numerical calculations when using the arctan function. The second departure is in the implementation of the solution. The original formulation of Sneddon and Elliott (1946) is for a semi-infinite fracture (i.e. referring to Fig. 4, the fracture is assumed to have a total height, h, and infinite length in-and-out of the plane).

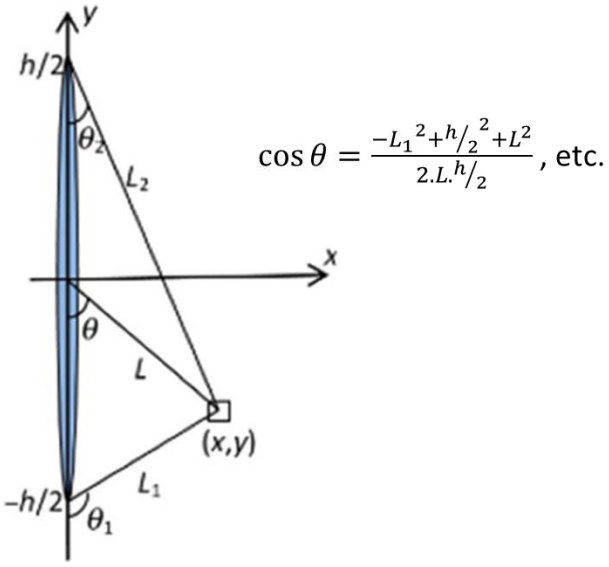

Fig. 4. Schematic of a 2D fracture

As the Duvernay analyses covered here are two-dimensional in the horizontal plane, the Sneddon and Elliott equations are applied with the fractures having a total *length* of h and an infinite height. This is considered an acceptable assumption in the early phase of the development of this technology. (Analyses need to be extended into three-dimensions to consider stress interaction effects between wells with different landing zone depths.)

Figure 5 shows the effects of superposition of normalized stress changes perpendicular to three fractures having half-length and spacing of unity. In between the stages the combined effect results in a stress change approximately 2.3-times that of a single fracture. At distances beyond (i.e. outside) of the stimulated zone stress changes perpendicular to the fractures can be slightly negative.

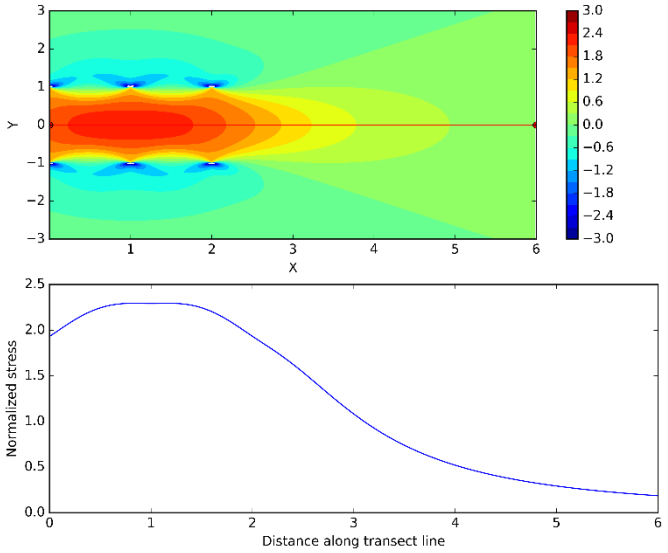

Fig. 5 Normalized stress changes perpendicular to three idealized fractures of half-length of unity.

With this basic understanding of the 'stress shadow effect' in place, stress changes both perpendicular and parallel to the created hydraulic fractures can then be predicted on a pad-scale within the area of interest, taking into account the stress-interactions between the many fracture stages pumped. (Stress changes in the vertical direction, and also shear stresses are also calculated, though these are significantly smaller in magnitude than stress changes parallel and perpendicular to the hydraulic fracture.) During the fracturing operations the fracture propagation azimuth is assumed to remain constant (roughly NE-SW), perpendicular to the Shmin-direction, with little reorientation.

In undertaking the stress-effects calculation it is useful to visualize the well stage fracturing order graphically (Figure 6). Wells were drilled north-to-south, with the toe of the well at the south.

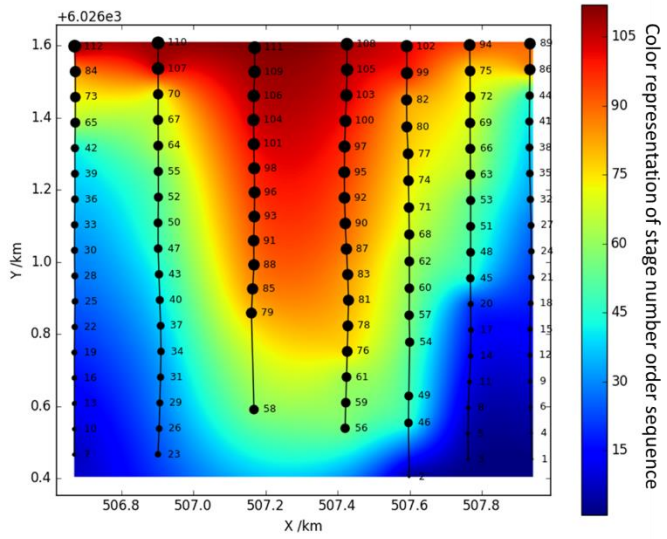

Fig. 6. Sequence order of well fracturing operations

With each well typically building a permanent 8 MPa stress shadow from 16 hydraulic fracture stages, analyses can be performed assuming superposition to derive the resultant changes in stress, both perpendicular and parallel to the induced fractures over the area of interest. Figure 7 shows an example analysis for stress changes perpendicular to the fractures (having a half-length of 160 m) at the end of the stimulation sequence. Note that due to the superposition effects of the spatially distributed hydraulic fractures, the resulting stress perturbation is not uniform. Perturbations, both perpendicular and parallel to the induced hydraulic fractures, vary both spatially and temporally during the well fracturing sequence.

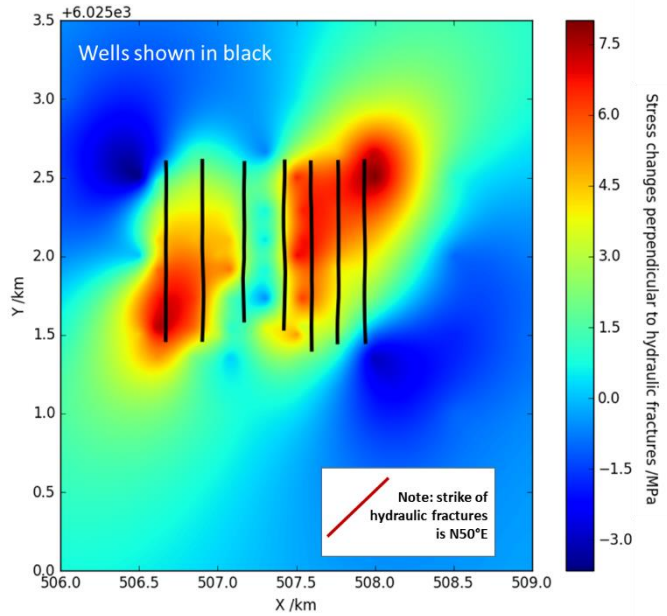

Fig. 7. Stress changes occurring perpendicular to created hydraulic fractures at the end of stimulation

3.2. Fluid Pressure Changes

During stimulation operations pore pressure changes also occur as a consequence of fluid leak-off from the fractures. The amount of fluid pumped during hydraulic fracturing operations can be large, even though the volume of fluid penetrating the formation is small, due to the low permeability. Total injected volumes are considered by some to be important indicators of the maximum size of possible IS events (McGarr, 2014; Schultz et al, 2018), and so this effect is included in the analyses. It should also be noted that much prior work has focused on IS caused by fluid diffusion (e.g. Shapiro and Dinske, 2009), and work presented here builds upon this framework.

DFIT analysis interpretations in the Duvernay indicate a fluid efficiency of about 92% (i.e. 8% of fluid pumped is injected into the formation). Typical stage injection volumes are 2250m^3, with injection operations lasting about 3 hours per stage. Therefore, fluid is injected into the formation at an approximate rate of 1 m^3/min. for the duration of pumping.

In the analysis of fluid diffusion a point source of injection is assumed coinciding with the stage location of the well that is being stimulated (Theis, 1935). Injection effects from the stimulated stage are superimposed on the diffusing pressure field generated by prior injections. The effective permeability of the formation is chosen such that the point source injection pressure is at fracturing pressure. This is recognized as a simplifying assumption for these initial analyses. Further work could extend the analyses to include an elliptical fluid invasion zone surrounding the hydraulic fracture, e.g. by analogy to thermal conduction (Perkins and Gonzales, 1985).

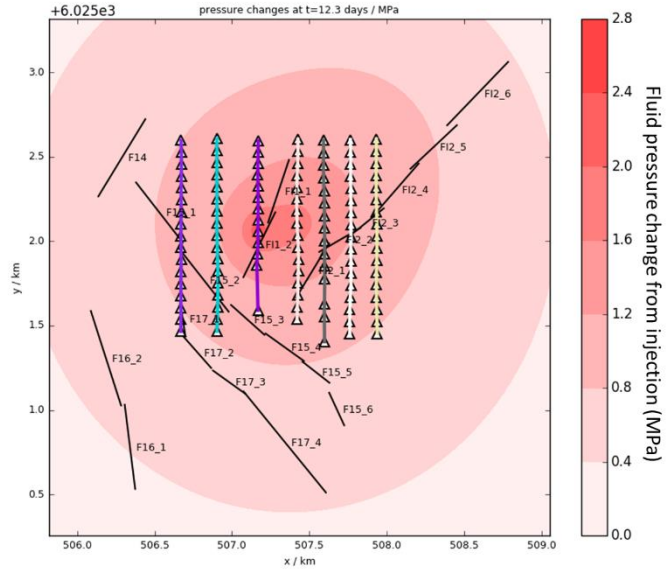

Fig. 8. Fluid pressure changes occurring at the time of stimulating Stage #91

The simulated fluid pressure distribution in the Section 26 Pad area 12.3 days into the injection operations is shown in Figure 8. Injection is taking place in Stage #91. (See Fig. 6 for location and ordering.)

It should be noted that the induced pressure changes are close to the estimated in-situ effective horizontal stress (3.81 MPa), giving an early indication that conditions may be favorable for fault slip under appropriate stress conditions. (Fault segments shown in Fig. 8 are discussed later in the paper.)

4. INITIAL SCREENING FOR IS

4.1. Fault Stability Analysis

3D seismic interpretations identified 32 fault segments of relevance to the Section 26 area (Figure 9). These were classified as those limited to the sedimentary interval only (15 faults, with prefix D) and those extending into the basement (17 faults, with prefix B). Each segment was assigned an average dip and strike angle appropriate for that fault segment.

Knowing in-situ stress conditions appropriate for the Duvernay wells' landing zone depth, and the fault segment orientations, initial fault stability analyses utilize a Mohr's Circle representation of stresses resolved onto the fault planes (Jaeger and Cook, 1969; Zoback and Townend, 2001; Zoback, 2010). The results are shown in Figure 10.

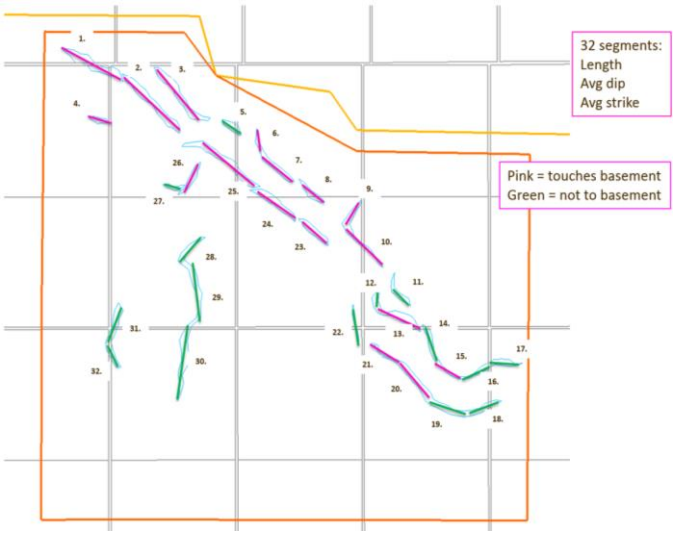

Fig. 9. Fault segments used in stability analysis.

Frictional bounds of 1.0 and 0.6 are shown according to Byerlee (1978), together with the average coefficient of friction of 0.74 established from rock mechanical testing on Duvernay core material. Only one fault is identified as being critically stressed in the prevailing stress state (fault D16), though five other faults close to the μ=0.6 frictional limit line are identified as being 'at risk'. This first level of screening thus allows an initial traffic-light assessment of fault stability - and hence IS - hazard (Figure 11).

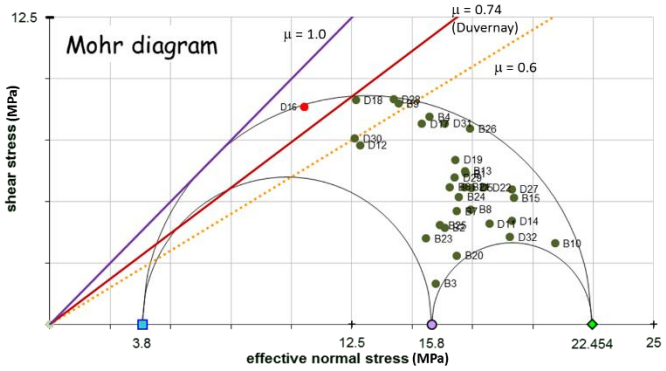

Fig. 10. Mohr's Circle analysis of fault stress conditions

This initial screening, incorporating readily available data, provides the foundation for more sophisticated analyses. Indeed, the ability to undertake this initial screening is now made far more accessible following the release of the Fault Slip Potential (FSP) tool (Walsh et al., 2017). Use of the FSP software permits probabilistic fault stability analyses (Walsh and Zoback, 2016) to more fully incorporate uncertainty in in-situ property values.

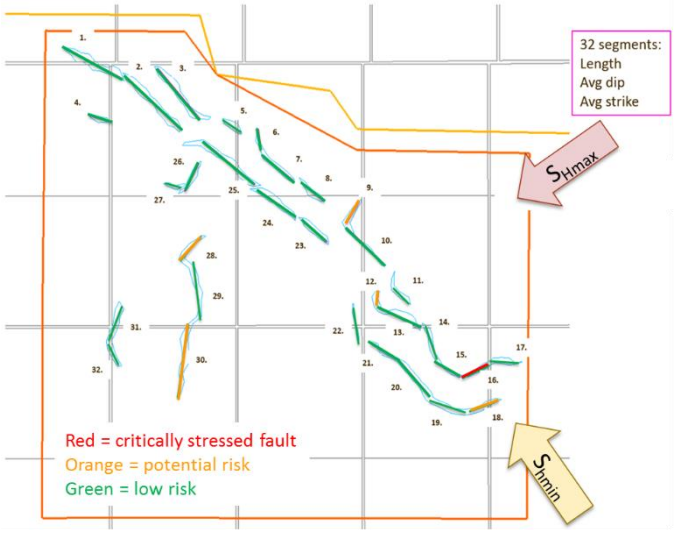

Fig. 11. Results of initial screening of fault slip hazard

4.2. Extended Fault Stability Analysis

As part of an evolving assessment of IS hazard utilizing analyses of increasing sophistication, fault stability analyses were extended to include a more representative 3D topological description of fault architecture. This capability is available in most subsurface modeling software available from major vendors. Analysis of two adjacent fault segments B9 and B10 is described here for illustration purposes, though in our assessment of IS hazard all faults were treated similarly. (See Fig. 9 for location.) Fault B9 is close to being critically stressed, requiring only 2.39 MPa pressure change to make it slip

(based on average fault properties, Fig. 10), whereas fault B10 is far from being critically stressed, requiring a 16.46 MPa pressure change.

Fault geometries picked on seismic are not as linear as shown in Fig. 9. Use of the picked geometry (even though subject to some error) allows analyses to advance beyond a simple linear representation of fault geometry. In this case, fault surfaces were discretized into numerous equilateral triangles of 10 m side length, each with its own local dip and strike direction. Fault stability analyses are then performed on each individual triangular element (Figure 12). Also shown is an example horizontal well path. This crosses fault segment B10 at a location requiring a large pressure change for fault slip to occur (approximately 15 MPa). The fault stability analysis shown in Fig. 12 may, therefore, also be used in well planning so as to avoid fault intersections where instability and losses may be a risk. (See Willson et al, 2007, for more consideration of these issues.)

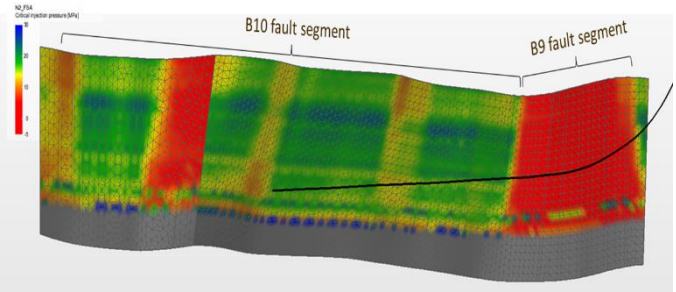

Fig. 12. Stability of fault B10 & B9: change in stress or pore pressure (MPa) for the fault to slip

Statistical summaries of pressure changes required for fault slip can be made (Figure 13), and these show that the detailed 3D analysis of fault discretization triangles is in close agreement with simple analytical Mohr Circle analysis of pressures necessary for fault slip.

In these extended analyses of fault stability, two analyses are performed using a Discrete Fracture Network (DFN) that attempts to represent mapped faults in the area of interest as well as incorporating faulting and fracturing on a sub-seismic scale. The first analysis is for undisturbed initial stress conditions. The second analysis superimposes on the faults pressure and stress changes caused by hydraulic fracturing operations.

Calculated stress changes from fracturing are resolved into normal and shear stress changes using transformation matrices given in Jaeger and Cook (1969). The fault stability analyses are re-run for this perturbed stress state. Statistics of shear stress ratio on the discretized fault segments are generated, similar to that shown in Figs. 12 and 13. (Here a ratio greater than 1 indicates the fault is critically stressed.) Differencing the two solutions provides the number of discretized fault triangles in the perturbed state whose shear stress ratio has increased above 1. In the full analysis of all faults, 2085 triangles have their shear stress ratio increased to beyond 1 as a result of pressure and stress changes resulting from Section 26 pad stimulation operations. Knowing the triangle discretization dimensions, this is equivalent to a fault slippage length of 340 m, *assuming all events occurred on one plane simultaneously*.

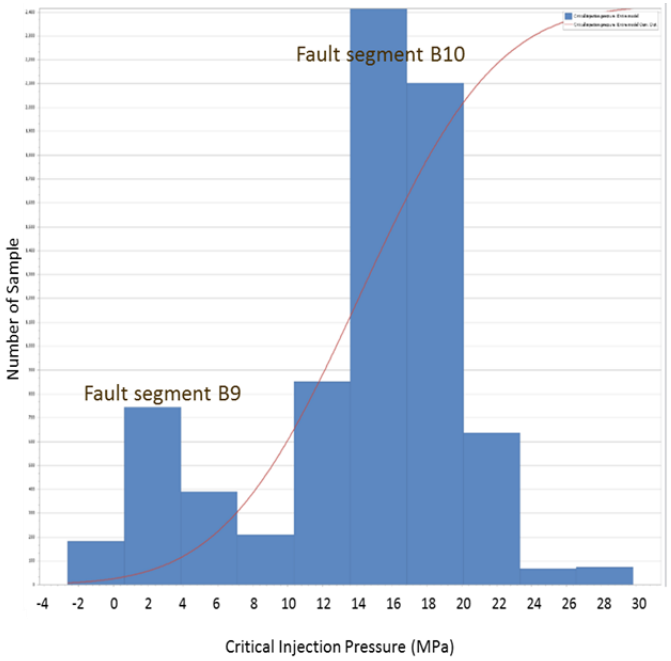

Fig. 13. Summary of pore pressure change needed for slippage on fault B10 & B9

This, obviously, is a big assumption to make, but it does permit an estimation to be made of the maximum single equivalent IS event size that might be possible – see Figure 14.

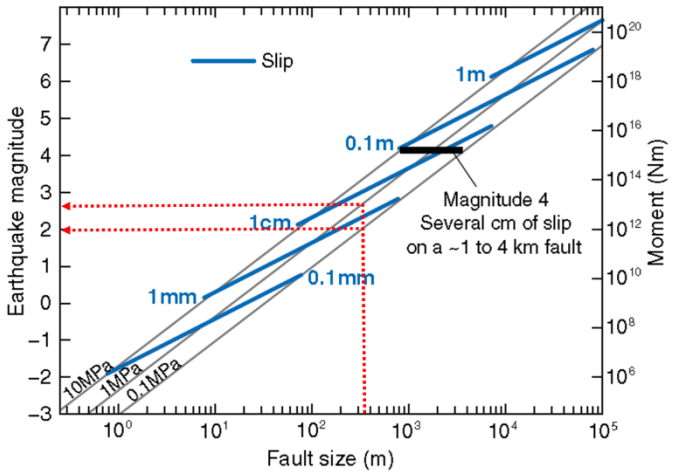

Fig. 14. Relationship between fault slip length and earthquake magnitude (modified from Zoback and Gorelick, 2012)

For typical stress drops associated with earthquake events, it is estimated – for the stress state and fault geometry considered – that the seismic energy release, at

most, would be equivalent to that of a single M_L 2.0 to 2.6 event. Analyses of this type do provide some reassurance for hazard screening, as the single equivalent IS event size is lower than that specified by Regulators for cessation of operations (M_L4.0).

One can imagine a more severe scenario where fault orientations and stress conditions are less benign than in the Section 26 area. Here, analyses such as these could predict a much greater fault slip area as a consequence of imposed stress and pressure perturbations such that slippage on a combined fault segment of the order of 1-4 km might be possible, so potentially creating a M4.0 event.

Extending this analyses further to consider seismic energy release, Gutenberg and Richter (1956) provide the following relationship between seismic moment (surface wave magnitude, M) and energy (E, in ergs):

$$\mathbf{Log_{10}E = 1.5M + 11.8} \qquad (1)$$

The energy equivalent of the cumulative microseismic events recorded during stimulation of the Duvernay Section 26 pad (Figure 15) can thus be calculated. The total energy release from the 118,604 events recorded at the Section 26 pad is equivalent to 1.18×10^{15} ergs (118 MJ) energy release. Equating this to a single IS event yields a possible Magnitude 2.2 event. This is in close agreement with the Magnitude 2.0-2.6 event size range possible from the fault slippage analysis considered above. In this way, we believe that conventional fault slippage analysis can be extended to assess the *potential* for a single larger IS event occurring. If events of concern are speculated by such an analysis this could provide justification of additional monitoring or contingency measures to be put in place during hydraulic fracturing operations.

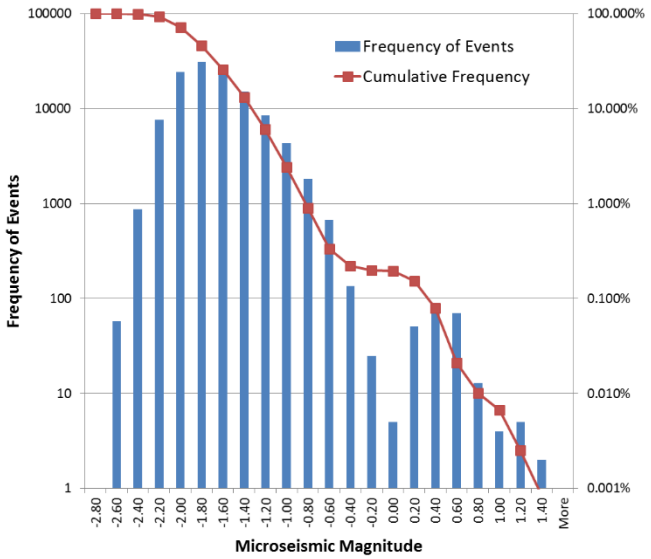

Fig. 15. Cumulative histogram of all microseismic events recorded when stimulating the Duvernay pad.

5. ADVANCED ASSESSMENT OF IS

Though encouraging, the limitations and assumptions inherent in the fault stress state analyses described above were recognized. In particular, although the stress ratio analysis can identify areas of faults where earthquake triggering is possible, more work is required to understand whether fault rupture can extend outside these areas. Ideally a model capable of *probabilistically predicting* the range of possible IS events is required. At the time the fault stability work was underway (late-2016 to early 2017) a new simulation approach was published – by Dempsey and Suckale (2016) and Dempsey et al (2016). As noted in this latter reference:

"Probabilistic seismic hazard assessment for induced seismicity depends on reliable estimates of the locations, rate, and magnitude frequency properties of earthquake sequences. The purpose of this paper is to investigate how variations in these properties emerge from interactions between an evolving fluid pressure distribution and the mechanics of rupture on heterogeneous faults."

At first reading, these simulation tools offered the possibility of extending the fault stability work into the calibrated predictive realm. This kind of calibration and scenario-forecasting was recently demonstrated for 325 faults in the Groningen gas field in The Netherlands (Dempsey and Suckale, 2017). Through a short-term collaborative agreement with the University of Auckland the Python-scripted QK1 code was applied to the Section 26 pad hydraulic fracturing scenario. The results of these initial analyses are reported here.

5.1. Theoretical Framework

A detailed recapitulation of the physics and algorithms underpinning QK1 is beyond the scope of this paper – the reader is referred to the original JGR publications. A brief description only is provided here.

Faults are modeled as an ensemble collection with arbitrary shear stress heterogeneity repeatedly drawn from a random distribution with user-specified mean, standard deviation and spatial correlation parameters. The model simulates the location of the earthquake hypocenter triggered by arbitrary pressure and stress loading and assuming a slip-weakening instability criterion (Uenishi and Rice, 2003). In Dempsey et al (2016) only perturbations in pressure arising from multiple point-source fluid injections were considered. As part of the collaboration, the fault loading was modified to include spatially- and temporally-evolving shear and normal stresses resulting from the hydraulic fracturing 'stress shadow' effects described in Section 3.

The model is 1D – requiring only that the fault trace coordinates be defined. (Imposed shear and normal stresses do account for fault strike and dip, however.) This approach is attractive as integral solutions for 1-D

fracture propagation exist (e.g., Eshelby, 1969; Rice, 1980), which reduces the computation time, enabling large earthquake catalogs (>10^5 events) to be simulated and parameter uncertainty to be explored. Upon triggering slip due to the imposed stress and pressure changes, fracture propagation is simulated using a concept of energy sources and sinks until such time that fracture propagation arrest criteria are met (Figure 16).

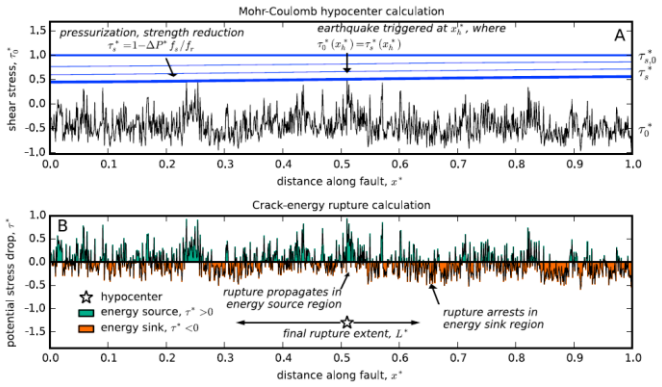

Fig. 16. Event hypocenter location and fault rupture length assessment (from Dempsey and Suckale, 2016)

Applying this technique to the evolving stress and pressure state during the simulation, a catalogue of event timings, locations, rupture lengths, stress-drops and energy release is thus generated. Seismogenic parameters used to construct the event magnitude frequency distribution are then calibrated to field observations of microseismicity and induced seismicity to produce the appropriate observed Gutenberg-Richter relationship.

5.2. Calibration to Section 26 Microseismic

The larger Smoke Lake seismic area with identified faulting (Fig. 9) was reduced to smaller size for the detailed analysis of microseismic events. Picked faults were also supplemented by faults at the limit of seismic resolution that were illuminated by microseismic data. Fault segments used in the analyses are those shown in Fig. 8. Short length discretization was imposed by the stress loading algorithm implemented in the code at that time. However, the minimum fault length selected (at least 500 m) ensured that any segment had the potential to generate at least a Magnitude 3 event should the fault trace slip in its entirety (e.g. by reference to Fig. 14).

Through an iterative process the observed Section 26 pad microseismic catalogue of events -1M and larger was matched by the model (Figure 17). (An inherent assumption in QK1 is that all modeled events are occurring on faults.) In Fig. 17 the curve represented by the black dots represents the full catalogue prediction, generated by the summation of individual catalogues from faults experiencing slip (colored dots). The solid line shows the actual monitored Duvernay events. (Note that the paucity of data collected in the M-0.6 to M0.0 range results from a geophone sampling bias.) Overall the match is considered to be very good, with the largest simulated event of M1.2 agreeing well with the largest recorded event of M1.26.

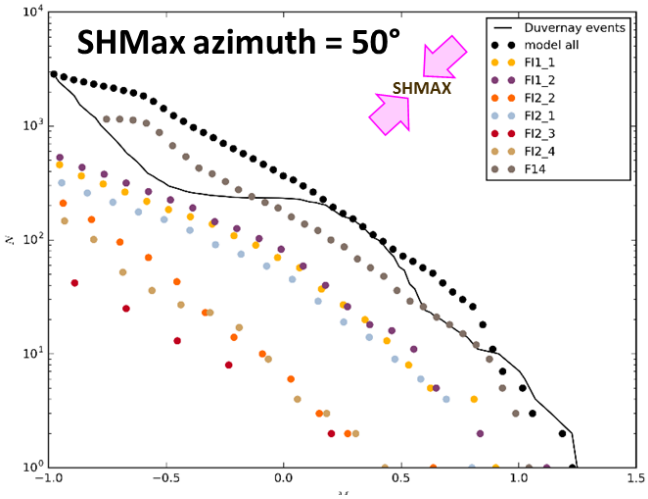

Fig. 17. Base case calibration for Section 26 pad microseismic – Largest event = M1.2

The flexibility of the Python scripting enables multiple displays of the evolving IS event catalogue – both spatially (as in Fig. 18), temporally for individual faults (as in Fig. 19), and also the relative contribution of seismicity from individual faults (as in Fig. 20).

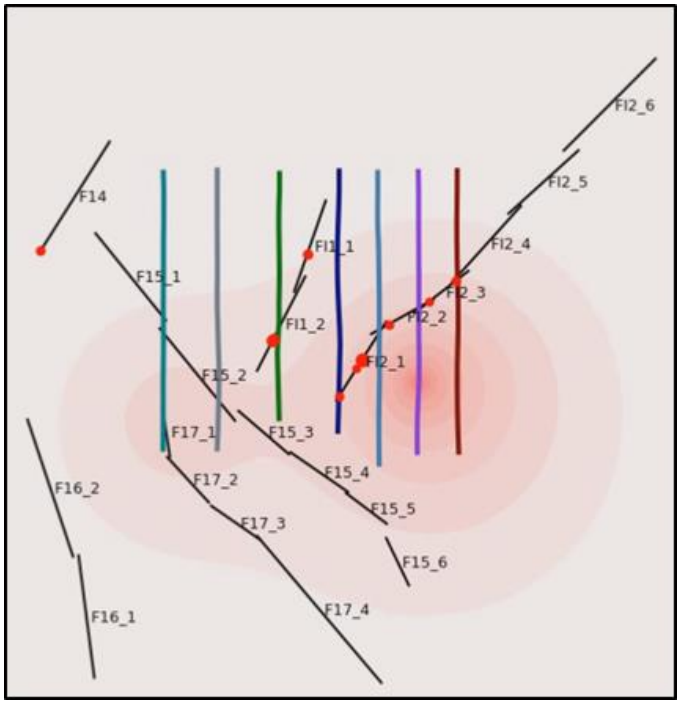

Fig. 18. Pressure diffusion map and induced seismicity (red dots) after completing Stage #17 (dots are scaled by event magnitude)

The ability to interrogate the data generating the full event catalogue helps ensure adequate discretization of the problem and the identification of spurious events. They also enable a 'sense check' of the results and a developing understanding of the seismogenic process.

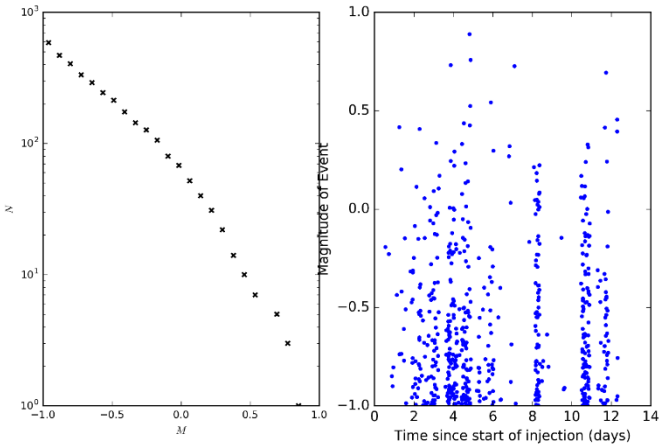

Fig. 19 Summary of Gutenberg-Richter magnitude vs. time output for a selected fault

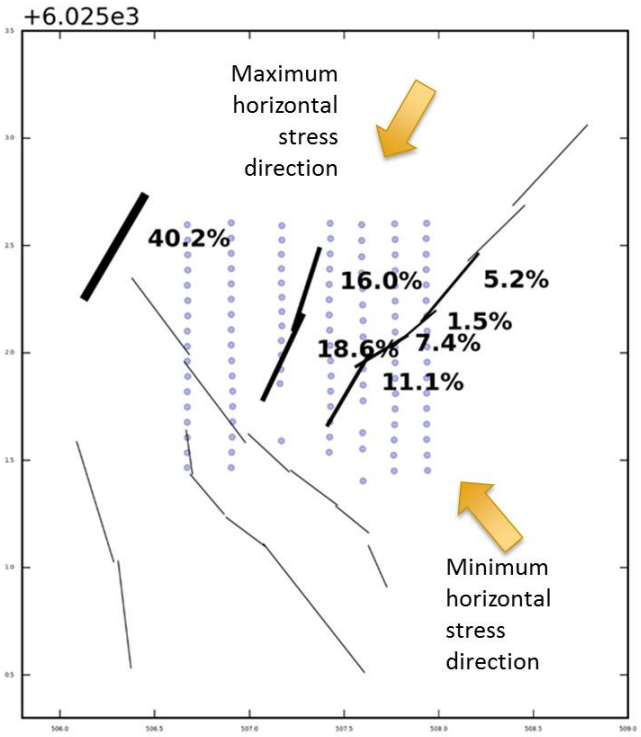

Fig. 20. Contribution of individual faults to the overall seismic catalogue (line width signifies relative contribution).

For example, in Fig. 20 it is easy to understand why faults striking in the direction of the minimum horizontal stress are aseismic. They are 'clamped' by the action of the maximum horizontal stress acting almost perpendicular to them. It should also be noted that fault segment "F14" contributing most of the seismicity is the same "B9" fault segment identified as being 'at risk' in screening analyses reported in Section 4 of this paper. Segment B10, requiring a large pressure change to cause fault slippage in those analyses, is represented in the advanced analyses by the six individual segments of Fault "F15". (See fault labeling in Fig. 18.) Thus, a direct linkage can be established between both the simple and advanced analyses of fault stability.

5.3. Scenario Modeling

Having calibrated the model for the Section 26 pad location, it is now possible to undertake scenario modeling to assess the IS hazard at other locations. The close proximity of leased acreage and relatively consistent formation depth for the Duvernay (at least over the immediate geographic area) makes it realistic to assume that the calibrated factors are valid in neighboring areas. In the following sections, a series of 'what-if' analyses are presented to illustrate this process.

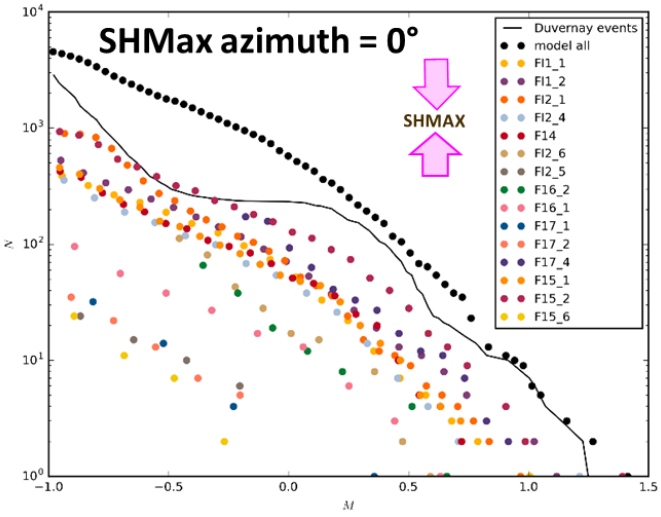

Fig. 21. Forecasted microseismic event catalogue for a North-South stress orientation – Largest event = M1.4

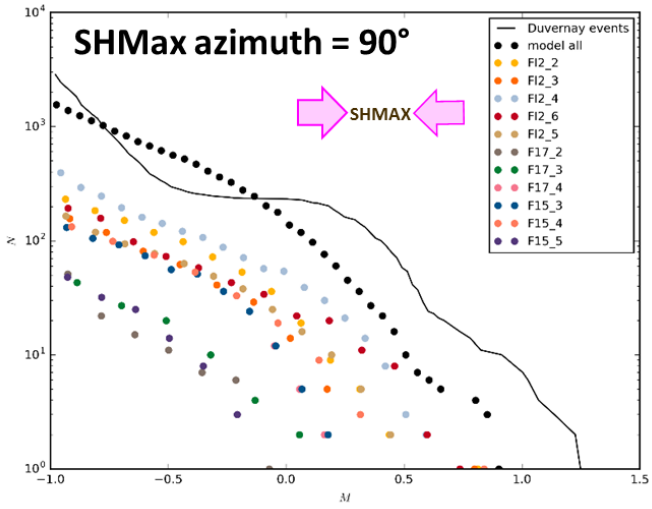

Fig. 22. Forecasted microseismic event catalogue for an East-West stress orientation – Largest event = M0.9

5.3.1.Influence of Stress Azimuth

One straightforward scenario to model is having a different maximum horizontal stress azimuth relative to the major faulting. While in reality the maximum horizontal stress direction remains fairly constant in Western Canada and the fault orientations change due to the change in the reef-edge profile (Schultz et al, 2016),

numerically it is most expeditious to fix the fault orientations and to change the stress direction. Figures 21 and 22 present analyses for maximum horizontal stress directions of North-South and East-West. Not only does the largest forecasted event change, but those faults contributing to the overall catalogue also changes – compare Fig 20 with Fig. 23 for example.

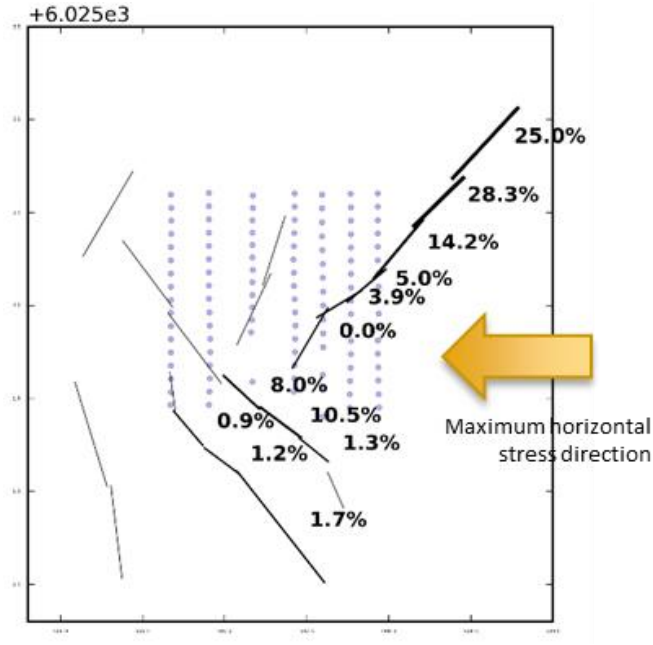

Fig. 23. Contribution of individual faults to the overall seismic catalogue for an East-West stress direction. (Line width signifies relative contribution. Largest event = M0.9)

5.3.2.Influence of Stage Ordering

Another factor of relevance to operations is the order in which the well fracture stages are performed. Fig. 6 shows the sequence of fracturing implemented at the Section 26 pad. Here a modified form of 'zipper fracturing' is used, with successive stages moving between wells. In the simulations it is easy to alter the well sequencing – e.g. completing the leftmost well A first and then progressing in well order to the rightmost well G (Figure 24), or by reversing this order (Figure 25). Maximum horizontal stress direction is maintained at 50° in these simulations.

The results of differing the stage ordering are potentially significant, as injection parameters (volume, duration and rate) remain unchanged, yet the largest forecasted event is greater in both cases where sequential fracturing is simulated, compared with the base-case zipper fracturing scenario. This is due to the concentration effect of sequential fracturing – i.e. many stages in close proximity, both spatially and temporally – compared to the zipper fracturing scenario where greater pore pressure diffusion occurs between stimulating adjacent stages. However, further analysis is required to establish whether this trend exists above the statistical noise (aleatoric uncertainty) inherent in earthquake triggering situations, and the extent to which simulations may be exacerbated by individual occurrences of larger magnitude events.

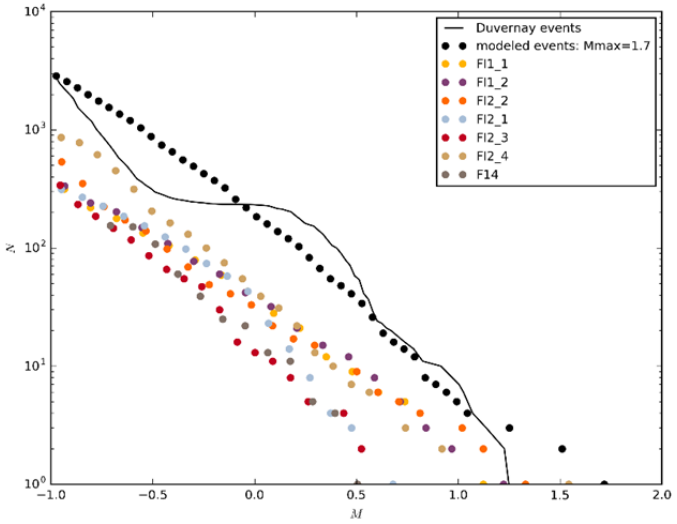

Fig. 24. Forecasted microseismic event catalogue for a Well A through G completion sequence – Largest event = M1.7

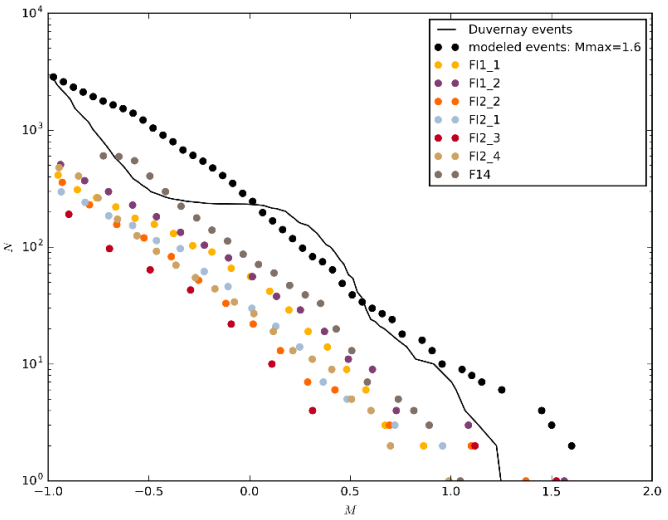

Fig. 25. Forecasted microseismic event catalogue for a Well G through A completion sequence – Largest event = M1.6

5.3.3.Influence of Reservoir Pressure

Depending on location and hydrocarbon fluid phase-type, pore pressure can vary significantly over the greater Duvernay Fairway (Lyster et al, 2017, Figure 26). Studies by Bachmann et al (2012); Eaton (2017); Eaton et al (2017) and Schultz et al (2018) all point to increased risk of IS where pore pressure is elevated. This is quite understandable in terms of the Mohr Circle analyses presented in Section 4 of this paper, as initial effective stresses are reduced.

The 'base case' seismic response calibration shown in Fig. 17 used a pore pressure of 53.84 MPa, equivalent to a gradient of 17.37 kPa/m. Here the forecasted maximum event size of M1.2 agreed with the observed microseismicity. Additional scenarios were analyzed with a pore pressure gradient of 18.0 kPa/m (Fig. 27) and 18.6 kPa/m (Fig. 28). It was not possible to undertake analyses at higher pore pressure gradients than this, as at the time QK1 was unable to handle a tensile failure condition.

These results clearly show the impact of elevated pore pressure on IS event magnitude, which may be incorporated into more advanced IS traffic-light protocols.

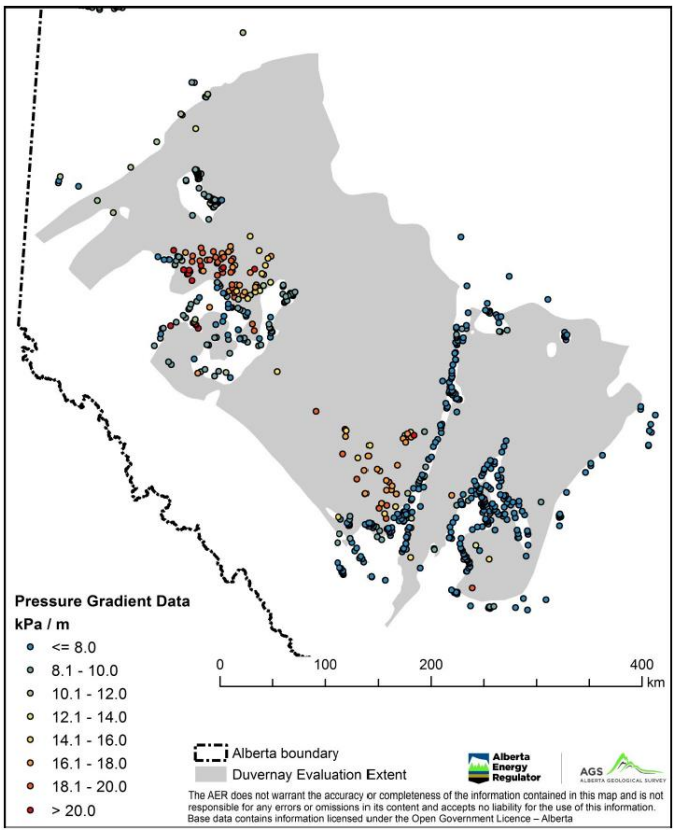

Fig. 26. Duvernay pore pressure (from Lyster et al, 2017)

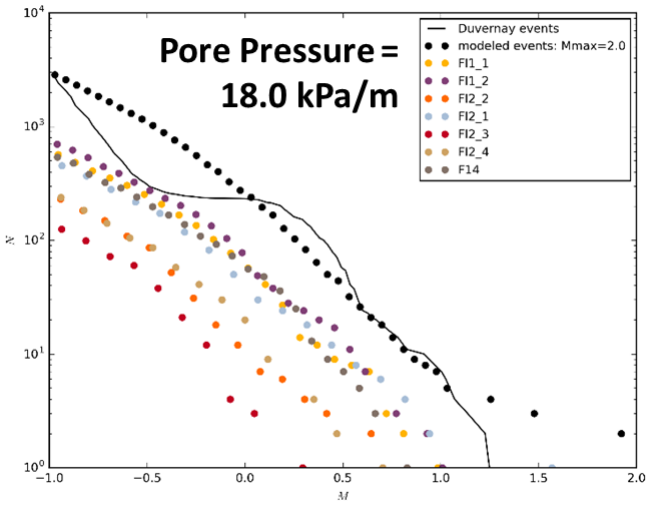

Fig. 27. Forecasted microseismic event catalogue for pore pressure gradient of 18.0 kPa/m – Largest event = M2.0

6. CONCLUSIONS

A workflow has been presented that permits a staged assessment of induced seismicity hazard of increasing sophistication. The simplest Mohr Circle analyses can be performed using readily available subsurface data – either from published or open-source information (e.g. Bell and Grasby, 2012; Lyster et al, 2017) or from proprietary studies. Recently-available open-source software tools (Walsh et al, 2017) now enable the application of this analysis without recourse to proprietary software.

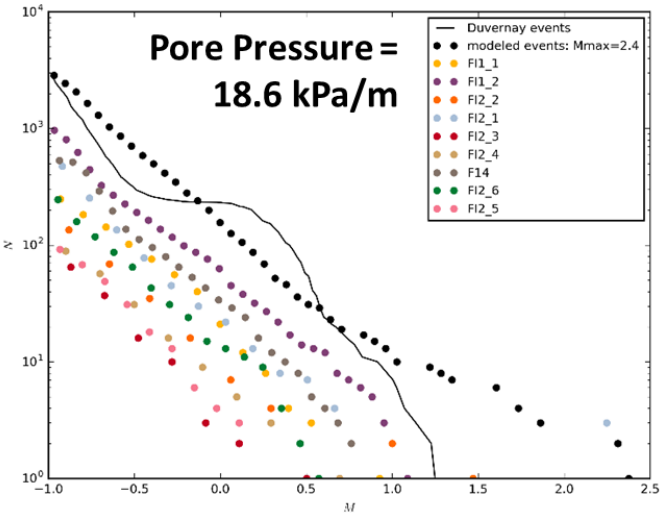

Fig. 28. Forecasted microseismic event catalogue for pore pressure gradient of 18.6 kPa/m – Largest event = M2.4

The extended fault stability analysis described in Section 4.2 is also considered to be within reach of many operators, as most use subsurface modeling packages from the major vendors that include this capability (though possibly not always within the standard platform of options). The ability to assess the extent of fault slippage from injection and stimulation operations, and potentially relate this to maximum possible single event size, is considered to be a useful next step in the hazard screening process.

The results of QK1 modeling still under development look particularly promising. Applying the model to the Section 26 pad produced simulated results that agreed with the highest magnitude event recorded in the field. While a priori prediction of induced seismicity is still not possible, the practicality of 'calibrated forecasting' and scenario modeling based on analyses of well-documented prior well stimulations does appear to be quite viable, with useful insights gained. The interaction of key drivers for IS events of significance – injection volume, fault geometry, and stress and pressure – can more easily be separated and considered in isolation. The Authors of this paper look forward to future developments in due course.

REFERENCES

Alberta Energy Regulator, 2015. Subsurface Order No 2: Monitoring and Reporting of Seismicity in the Vicinity of Hydraulic Fracturing Operations in the Duvernay Zone, Fox Creek, Alberta, AER Bulletin 2015-07, 2015.

Atkinson, G.M., D.W. Eaton, H. Ghofrani, D. Walker, B. Cheadle, R. Schultz, R. Shcherbakov, K. Tiampo, J. Gu, R. M.

Harrington, Y. Liu, M. van der Baan, and H. Kao. 2016. Hydraulic fracturing and induced seismicity in the Western Canada Sedimentary Basin. *Seismol. Res. Lett.* 87, 631–647.

Bachmann, C.E., S. Wiemer, B.P. Goertz-Allmann, and J. Woessner. 2012. Influence of pore-pressure on the event-size distribution of induced earthquakes. *Geophys. Res. Lett*. 39, L09302.

Bao, X. and D.W. Eaton. 2016. Fault activation by hydraulic fracturing in western Canada. *Science* 10.1126/ science.aag2583.

BC Oil and Gas Commission. 2012. Investigation of observed seismicity in the Horn River basin, *Report of British Columbia Oil and Gas Commission.*

BC Oil and Gas Commission. 2014. Investigation of observed seismicity in the Montney Trend. *Report of British Columbia Oil and Gas Commission.*

Bell, J.S. and S.E. Grasby. 2012. The stress regime of the Western Canadian Sedimentary Basin. *Geofluids*, 12: 150–165.

Byerlee, J.D. 1978. Friction of rocks. *Pure and Applied Geophysics.* 116 (4-5): 615–626.

Clarke, H., L. Eisner, P. Styles, and P. Turner. 2014. Felt seismicity associated with shale gas hydraulic fracturing: The first documented example in Europe. *Geophys. Res. Lett.* 41, 8308–8314.

Davies, R., G. Foulger, A. Bindley, and P. Styles. 2013. Induced seismicity and hydraulic fracturing for the recovery of hydrocarbons. *Marine and Petroleum Geology* 45, 171-185.

Dempsey, D. and J. Suckale. 2016. Collective properties of injection-induced earthquake sequences: 1. Model description and directivity bias. J. *Geophys. Res. Solid Earth*, 121.

Dempsey, D., J. Suckale, and Y. Huang. 2016. Collective properties of injection-induced earthquake sequences: 2. Spatiotemporal evolution and magnitude frequency distributions. *J. Geophys. Res. Solid Earth*, 121.

Dempsey, D. and J. Suckale. 2017. Physics-based forecasting of induced seismicity at Groningen gas field, the Netherlands. *Geophys. Res. Lett.*, 44.

Eaton, D.W. and A. Babaie Mahani. 2015. Focal mechanisms of some inferred induced earthquakes in Alberta, Canada. *Seismol. Res. Lett.*, 86, 4, July/August 2015.

Eaton, D.W. 2017. Dynamics of fault activation by hydraulic fracturing in overpressured shales, in 79th EAGE Conference and Exhibition 2017 - Workshops (European Association of Geoscientists & Engineers, 2017).

Eaton, D.W., X. Bao, and B.A. Cheadle. 2017. Fault activation by hydraulic fracturing in overpressured shale formations. *Schatzalp 2nd Induced Seismicity Workshop*, 14-17 March 2017.

Ellsworth, W. 2013. Injection-induced earthquakes, *Science* 341, 1225942.

Eshelby, J.D. 1969. The elastic field of a crack extending non-uniformly under general anti-plane loading, *J. Mech. Phys. Solids*, 17, 177–199.

Friberg, P.A., G.M. Besana-Ostman, and I. Dricker. 2013. Characterization of an earthquake sequence triggered by hydraulic fracturing in Harrison County, *Ohio. Seismol. Res. Lett.* 85, 6 Nov/Dec.

Frohlich, C., W. Ellsworth, W. Brown, M. Brunt, J. Luetgert, T. MacDonald, and S. Walter. 2014. The 17 May 2012 M 4.8 earthquake near Timpson, East Texas: An event possibly triggered by fluid injection, *J. Geophys. Res*. 119, 581–593.

Green, C.A., P. Styles, and B.J. Baptie. 2012. Preese Hall shale gas fracturing: review and recommendation for induced seismic mitigation, https://www.gov.uk/government/publications/

Gutenberg, B. and C.F. Richter. 1956. Earthquake magnitude, intensity, energy and acceleration. *Bull. Seismol. Soc. Am.*, 46, 105-146.

Holland, A. 2011. Examination of possibly induced seismicity from hydraulic fracturing in the Eola field, Garvin County, Oklahoma. *Okla. Geol. Surv. Open-File Rept.* OF1-2011, 28 pp.

Holland, A. 2013. Earthquakes triggered by hydraulic fracturing in south-central Oklahoma. *Bull. Seismol. Soc. Am.* 103, 1784–1792.

Jaeger, J.C. and N.G.W. Cook. 1969. *Fundamentals of Rock Mechanics.* Methuen and Co., London.

Lyster, S., H.J. Corlett, and H. Berhane. 2017. Hydrocarbon resource potential of the Duvernay Formation in Alberta; Alberta Energy Regulator, AER/AGS Open File Report 2017-02, 44 p.

McGarr, A. 2014. Maximum magnitude earthquakes induced by fluid injection. *J. Geophys. Res.* 119, 1008–1019 (2014).

Perkins, T.K., and J.A. Gonzalez. 1985. The effect of thermoelastic stresses on injection well fracturing. *Society of Petroleum Engineers Journal.* February, pp. 78-88.

Rice, J.R. 1980. The mechanics of earthquake rupture, in *Physics of the Earth's Interior*, *Proceedings of International School Physics Enrico Fermi*, vol. 78, Dziewonski and Boschi Eds., pp. 555–649, North-Holland, Amsterdam.

Roussel, N. P., & M.M. Sharma, M. M. 2011. Optimizing fracture spacing and sequencing in horizontal-well fracturing. *SPE Production & Operations*, 26, 2 (SPE-127986).

Roussel, N. P. 2017. Analyzing ISIP stage-by-stage escalation to determine fracture height and horizontal-stress anisotropy. SPE Hydraulic Fracturing Tec. Conf. (SPE-184865).

Rubinstein, J., and A. Babaie Mahani. 2015. Myths and facts on wastewater injection, hydraulic fracturing, enhanced oil recovery, and induced seismicity, *Seismol. Res. Lett.* 86.

Schultz, R., H. Corlett, K. Haug, K. Kocon, K. MacCormack, V. Stern, and T. Shipman. 2016. Linking fossil reefs with earthquakes: Geologic insight to where induced seismicity occurs in Alberta. *Geophys. Res. Lett.* 43, 2534–2542.

Schultz, R., R. Wang, Y. J. Gu, K. Haug, and G. Atkinson. 2017. A seismological overview of the induced earthquakes in the Duvernay play near Fox Creek, Alberta. *J. Geophys. Res. Solid Earth*, 122.

Schultz, R., G. Atkinson, D. W. Eaton, Y. J. Gu, and H. Kao. 2018. Hydraulic fracturing volume is associated with induced

earthquake productivity in the Duvernay play. *Science* 359, 304-308.

Shapiro, S.A. and Dinske, C. 2009, Fluid-induced seismicity: Pressure diffusion and hydraulic fracturing, *Geophysical Prospecting*, 57, 301-310.

Skoumal, R., M. Brudzinski, and B. Currie. 2015. Earthquakes induced by hydraulic fracturing in Poland Township, Ohio. *Bull. Seismol. Soc. Am.* 105, 189–197.

Sneddon, I.N. 1946. The distribution of stress in the neighborhood of a crack in an elastic solid. *Proc. Roy. Soc. Lond. A*, Mathematical and Physical Sciences. 187, 1009, 229–260.

Sneddon, I.N., and H.A. Elliott. 1946. The opening of a Griffith crack under internal pressure. *Quart. App. Math.* 4, 3, 262–267.

Soliman, M.Y. and D. Adams. 2004. Geomechanics aspects of multiple fracturing of horizontal and vertical wells. 2004. SPE 86992, SPE Western Regional Meeting, Bakersfield, CA, USA

Switzer, S.B., Holland, W.G., Christie, D.S., Graf, G.C., Hedinger, A.S., McAuley, R.J., Wierzbicki, R.A., and Packard, J.J., 1994, The Woodbend-Winterburn strata of the Western Canada Sedimentary Basin, in Geological Atlas of the Western Canada Sedimentary Basin, G.D. Mossop and I. Shetsen, compilers: Geological Survey of Canada, Chapter 12, p. 165-202.

Theis, C.V. 1935. The relation between the lowering of the piezometric surface and the rate and duration of discharge of a well using groundwater storage, *Am. Geophys. Union Trans.*, 16, pp. 519-524.

Uenishi, K. and J. R. Rice. 2003. Universal nucleation length for slip-weakening rupture instability under nonuniform fault loading. *J. Geophys. Res.*, 108.

Walsh, F.R.I. III, and M. D. Zoback. 2016. Probabilistic assessment of potential fault slip related to injection-induced earthquakes: Application to north-central Oklahoma, USA. *Geology*. 44, 12, 991–994.

Walsh, F.R.I. III, M.D. Zoback, D. Pais, M. Weingartern, and T. Tyrell. 2017. FSP 1.0: A program for probabilistic estimation of fault slip potential resulting from fluid injection. https://scits.stanford.edu/software.

Walters, R. J., M. D. Zoback, J. W. Baker, and G. C. Beroza. 2015. Characterizing and responding to seismic risk associated with earthquakes potentially triggered by fluid disposal and hydraulic fracturing. *Seismol. Res. Lett.* 86, 1110–1118.

Weingarten, M., S. Ge, J. Godt, B. Bekins, and J. Rubinstein. 2015. High-rate injection is associated with the increase in U.S. mid-continent seismicity, *Science* 348, 1336–1344.

Willson, S.M., S.T. Edwards, A.J.L. Crook, A. Bere, D. Moos, P. Peska, and N.C. Last, N.C. 2007. Assuring Stability in Extended Reach Wells - Analyses, Practices & Mitigations, paper SPE/IADC 105405, SPE/IADC Drilling Conference, Amsterdam, The Netherlands.

Yew, C.H., and X. Weng. 2014. *Mechanics of Hydraulic Fracturing.* Second Ed., Gulf Professional Publishing, USA.

Zoback, M.D. and J. Townend. 2001. Implications of hydrostatic pore pressures and high crustal strength for the deformation of intraplate lithosphere. *Tectonophysics.* 336, 19-30.

Zoback, M.D. 2010. *Reservoir Geomechanics.* Cambridge Univ. Press, Cambridge, U. K.

Zoback, M.D. and S M. Gorelick. 2012. Earthquake triggering and large-scale geologic storage of carbon dioxide. *Proceedings of the National Academy of Sciences of the United States of America*, 109, 26, 10164 – 10168.